Modeling of the integrated magnetic focusing and gated field-emission device with single carbon nanotube

P.-Y. Chen, K.-H. Hsu, K.-W. Cheng, C.-T. Hung, J.-S. Wu, T.-C. Cheng, and J.-P. Yu

Modeling of the integrated magnetic focusing and gated field-emission device with single carbon nanotube

P.-Y. Chen, K.-H. Hsu, K.-W. Cheng, C.-T. Hung, and J.-S. Wu[a]
Department of Mechanical Engineering, National Chiao Tung University, Hsinchu 30050, Taiwan

T.-C. Cheng
National Nano Device Laboratories, Science-Based Industrial Park, Hsinchu 300, Taiwan

J.-P. Yu
Department of Information Management, Ming-Chuan University, Tau-Yuan 333, Taiwan

A gated single carbon nanotube field emitter with magnetic focusing is proposed and simulated using a parallelized Poisson's equation solver, coupled with the ray tracing of electrons, on an unstructured tetrahedral adaptive mesh. The magnetic focusing for the electrons can be achieved by a vertically downward magnetic focusing field $(-B_z)$ through the use of either external solenoids or permanent magnets around the field-emission array. The simulation results, assuming uniform magnetic field inside a field-emission unit, are compared with those conventional tetrode-type field emitters using an electrostatic focusing structure. The results reveal that the magnetic focusing design can promise much higher emission current, while a much smaller spot size results at the anode. In addition, the magnitude of the applied gate voltage in the range of 60–120 V shows little influence on the electron-beam diameter at the anode. The proposed magnetic focusing method can also possibly reduce the complexity of the fabrication without the electrostatic focusing structure. Noticeably, a distribution, similar to the Airy function, is obtained that shows the dependence of the spot size at the anode on the magnetic flux intensity. Thus, under suitable magnetic focusing conditions, it is possible to produce well-defined microelectron sources for many field-emission applications, such as novel parallel electron-beam lithography or field-emission displays. © 2007 American Vacuum Society. [DOI: 10.1116/1.2406064]

I. INTRODUCTION

Using carbon nanotubes (CNTs) as field-emission cathodes has attracted tremendous interest in the past few years for their remarkable field-emission (FE) properties such as high aspect ratio, whiskerlike shape for optimum geometrical field enhancement, high electrical conductivity, and extraordinary environment stability.[1–4] Therefore, CNTs have great potential to be used as field-emission cathodes for various applications of vacuum microelectronic devices, including field-emission displays (FEDs),[5–12] high-frequency microwave amplifiers,[13] electron microscopy, and parallel electron-beam lithography.[1,14]

Most of the FE devices applied the well-known Spindt-type structure,[15] which has a metallic or silicon etched field emitter with an integrated gate electrode aperture surrounding the emitter tip to control the extraction of emission current. The voltage applied on the gate electrode was typically larger than 70 V (Refs. 9–12) to extract the expected emission current for the operation of FE devices. Taking field-emission display applications, for example, a slightly higher current density, 5 μA, for a 355 μm pixel size is needed to stimulate the light emission from the phosphor at the anode.[9] The bias on the anode is typically between one to several kilovolts[9–12] to accelerate the electrons onto the anode. Field-emission cathodes based on multiple carbon nanotubes within the integrated gate electrode aperture have been reported in many papers over the past six years.[7–10,12,16] For some applications, such as electron-beam lithography and microscopy, an individual gated carbon nanotube field emitter was specifically fabricated to eliminate the screening effects and to optimize the emitted current and electron-beam diameter.[17–19] The electrons emitted from a very small area on the top of the CNT inherently spread with a large dispersion angle. Thus, an appropriate electron-beam focusing system is necessary for developing a well-focused electron-beam source.

Many numerical and experimental studies[11,20–22] indicated that it is most effective to use a focusing electrode above the gate electrode for controlling the electron trajectories. The voltage applied on the focusing electrode is always biased as zero,[10,11] negative,[10,12] or a few volts.[22] It was concluded that a concave structure having a larger focusing electrode aperture and a smaller gate aperture is favorable for less spreading of electron beams and for reducing the gate current.[10–12] However, the emission current can be greatly reduced and the gate leakage current will be oppositely increased due to this focusing electrode, which was not discussed in detail or was largely ignored in these studies.[11,21] Recently, the fabrication and operation of a single vertically aligned carbon nanotube with one integrated gate electrode and one focusing electrode have been demonstrated successfully via advanced
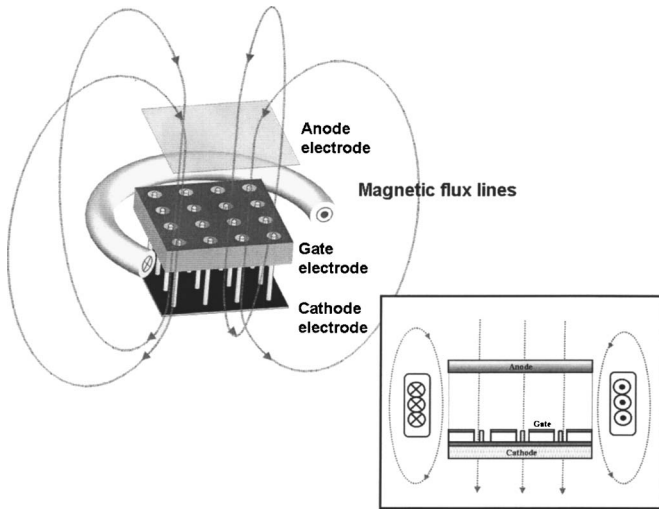

Fig. 1. Perspective view of the structure of the magnetic focusing carbon nanotube field-emission array.

microfabrication technology.[21,23] But these authors argued that the primary limitation of this type of device is the lack of device-to-device uniformity, due to fabrication precision, needed for some promising FE applications. Thus, an alternative means of electron focusing, instead of electrostatic focusing, has to be used to overcome these difficulties.

Remember that the magnetic focusing system is constantly used in electron optics/microscopy for its high focusability, stability, and simplicity in electron optics. In general, several permanent magnets or coils can be employed to produce a specific direction of magnetic field to confine the charged-particle trajectories. Based on the straightforward concept, a silicon field-emitter-array image sensor consisting of permanent magnets has been fabricated and demonstrated for its highly improved resolution.[24] Thus, a detailed understanding of the effects of the magnetic field to the electron-beam focusing in field emission can greatly benefit the research in this direction.

In this article, we intend to study via computer simulation how the electron-beam focusing effect varies with the applied magnetic flux density in a gated single carbon nanotube FE device. Results will also be compared with those obtained from the conventional tetrode-type FE device using the electrostatic focusing structure. The simulation model of the magnetic focusing structure consists of a solenoid (or a permanent magnet) outside the FE device, as shown in Fig. 1, which is used to induce the tunable magnetic flux density $(-B_z)$. For this type of device, uniformity of the magnetic flux intensity in space over the FE device is questionable; however, the assumption should hold for uniformity within a tiny field-emission cell (unit) on the order of 300 μm in width.

II. NUMERICAL METHOD

In the past, several numerical studies have been conducted for predicting field-emission properties.[10–12,20,21,25,26] Most of these studies use either the two-dimensional (2D) or

three-dimensional (3D) finite-difference method[10–12,20,21,25] or the 2D finite-element approach[26] for discretizing the electrostatic Poisson's equation. As mentioned earlier, a practical FED design often involves three-dimensional objects with a complicated geometry, rendering the use of the finite-difference method very difficult or unsuitable. The finite-element or finite-volume method using unstructured grids should represent the best choice for the numerical method. Also, the accuracy of the electron-flux prediction from the emitter strongly depends on the accuracy of the local electrical field near the emitter surface, which makes the grid resolution at the surface a critical issue in the simulation. This concern necessitates the use of an adaptive mesh refinement to achieve high accuracy in predicting the electrical field at the surface, which is the main concern of the current study.

In previous work,[27] we presented a parallelized 3D Poisson's equation solver using the finite-element method, coupled with a ray-tracing module, to predict field-emission properties of the gated field-emitter array with and without the electrostatic focusing structure by neglecting the space-charged effects. Space-charged effects can also be considered, which was demonstrated elsewhere.[28] In what follows, we only consider the case without space-charged effects.

Poisson's equation for the electrostatic distribution can be written as

$$\nabla^2 \phi = -\frac{\rho}{\varepsilon_0}, \tag{1}$$

where ϕ is the electric potential, ρ is the volume density of the free charges, and ε_0 is the permittivity of free space. Because the space-charged effects were neglected in the current study, Poisson's equation becomes a Laplacian equation,

$$\nabla^2 \phi = \frac{\partial^2 \phi}{\partial x^2} + \frac{\partial^2 \phi}{\partial y^2} + \frac{\partial^2 \phi}{\partial z^2}. \tag{2}$$

The Laplacian equation was discretized using the Galerkin finite-element method with an unstructured tetrahedral mesh for the flexibility of modeling objects with complex geometry. In the parallel implementation for Poisson's equation, a parallel conjugate gradient method is used to solve the resulting matrix equation using a geometrically nonoverlapping subdomain-by-subdomain (SBS) method.[29] The global coefficient matrix is stored in a compressed sparse row format as a partitioned matrix, and the dominant matrix-by-vector product and inner product of two vector operations of the coefficient matrix in the conjugate gradient method are performed on the SBS basis. In the current study, 20 processors are used for simulation throughout the study and the convergence criterion of the relative residual in parallel conjugate gradient is 10^{-7}, unless otherwise specified. In addition, a parallel multilevel graph-partitioning library[30] is used to partition the computational domain whenever necessary because the unstructured mesh is adopted in the current study.

A parallelized adaptive mesh refinement (PAMR) module[27] is coupled to automatically increase the accuracy of the predicted electric field near the tip of the field emitter.
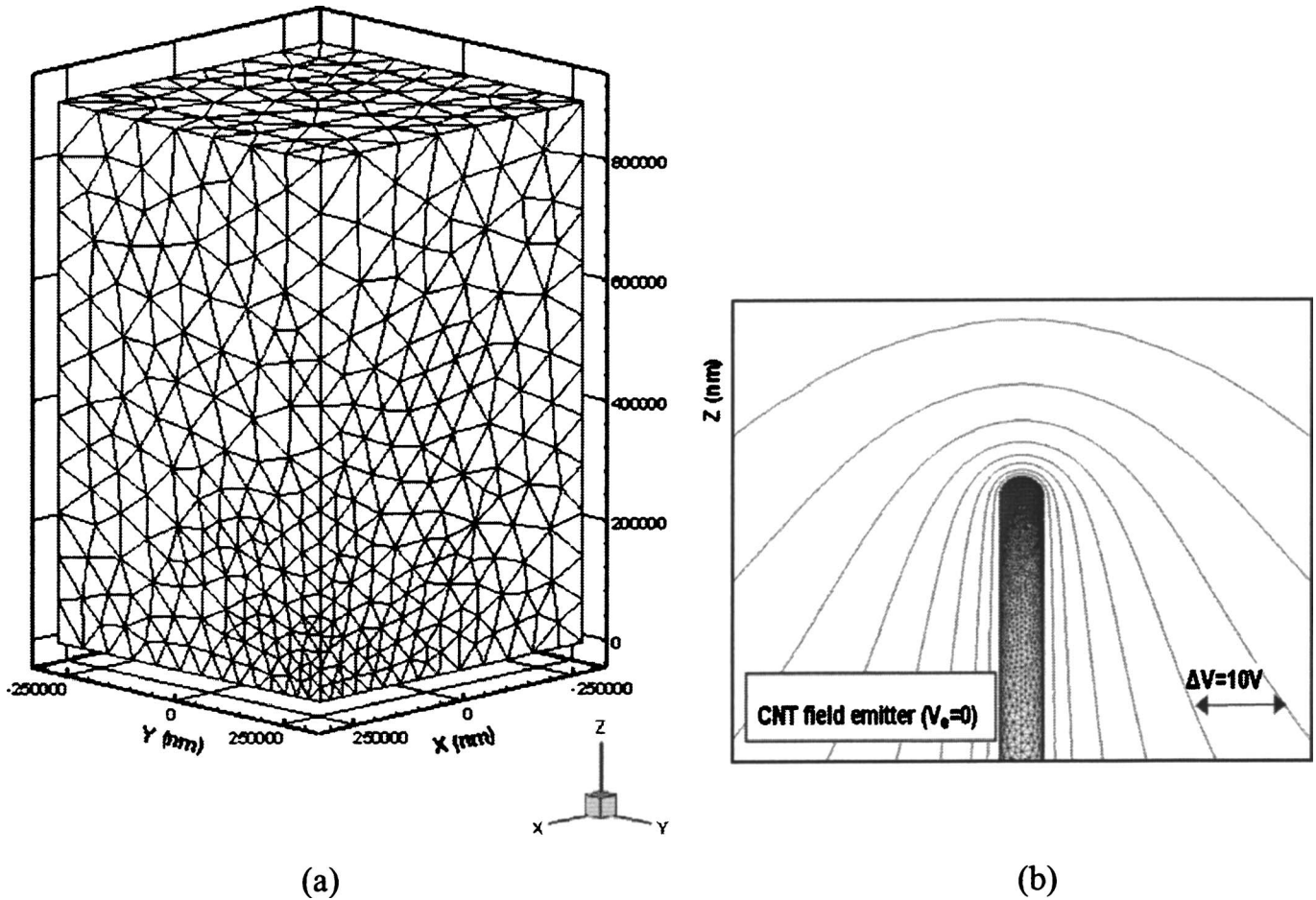
FIG. 2. (a) Typical surface mesh distribution of a single CNT triode-type field emitter within a periodic cell (1/4 of the full domain). (b) Exploded surface mesh distribution of the CNT field emitter and equipotential lines near the tip for $V_g=120$ V after five levels of mesh refinement (211 628 nodes and 1 044 771 tetrahedral cells).

In brief, PAMR is implemented using an *a posteriori* error estimator, as proposed by Zienkiewicz and Chu.[31] We have employed a very simple gradient recovery scheme by averaging the cell values of the FE solution to extract the "exact" solution of the electric field in each cell. A prescribed global relative error ε_{pre} of 0.0003 is used to control the level of accuracy throughout the study, unless otherwise specified. The absolute error in each element is then compared with a current mean absolute error at each level, based on ε_{pre}, to decide if refinement is required. In this case, an element is refined into eight child elements if required. Details of the implementation and study of the parallel performance can be found in our previous work.[27]

Figures 2(a) and 2(b) respectively show a typical view of the surface mesh distribution for the 1/4 cell and an exploded view of the refined surface mesh of the CNT field emitter using the PAMR (level 5) technique. The typical numbers of nodes and cells are about 0.2×10^6 and 1×10^6, respectively. After level-5 refinement, the maximum value of the electric field near the tip reaches an approximately constant value of 7.948 V/nm for $V_g=120$ V.

A modified Fowler-Nordheim emission model[32] is then inserted into the particle-tracing module, which traces the emitted electrons in the computational domain based on the E-field solution from Poisson's equation solver. The equation of the corresponding field-emission current density J to the normal component of the electric field at the emitter surface, E, in V/cm and the work function of the emitter, ϕ, in V [for a CNT, ϕ can be set to 5.0 eV (Ref. 16)] is

$$J = \frac{AE^2}{\phi t^2(y)} \exp\left(-B\frac{\phi^{3/2}}{E}\nu(y)\right)\frac{A}{cm^2}, \tag{3}$$

where

$$A = 1.5414 \times 10^{-6}, \tag{4}$$

$$B = 6.8309 \times 10^{7}, \tag{5}$$

$$y = 3.79 \times 10^{-4}E^{1/2}/\phi, \tag{6}$$

and y is the image charge lowering the contribution to the work function. The functions $t(y)$ and $\nu(y)$ are approximated by $t^2(y)=1.1$ and $\nu(y)=0.95-y^2$, respectively.

The emission current from each cell of the emitter surface is determined by the integral of the current density [Eq. (3)] using the local value of electric field at the emitter surface.
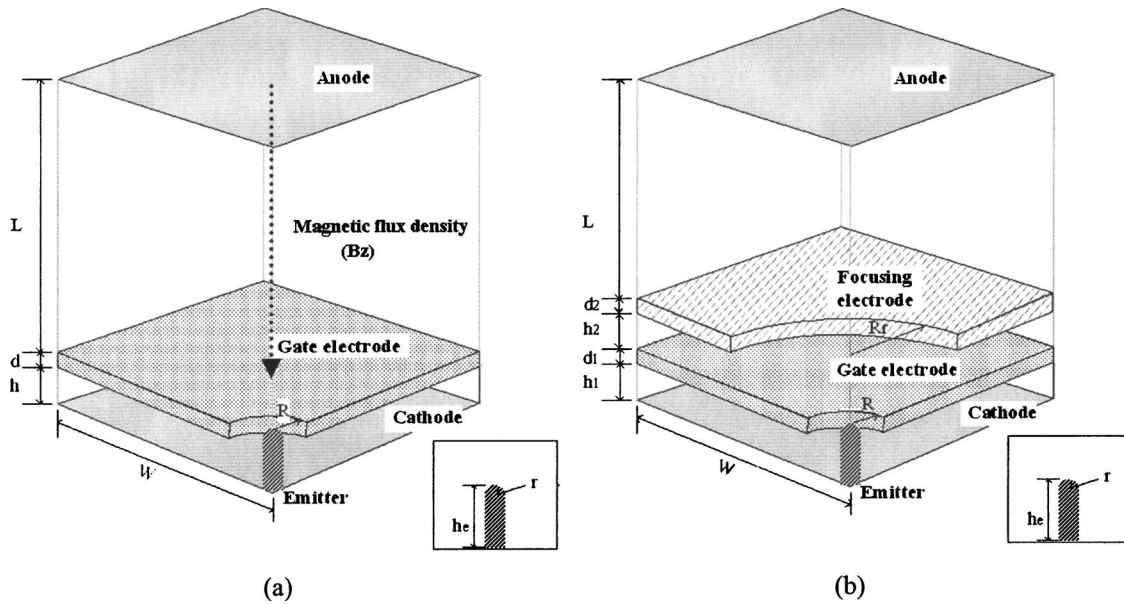
FIG. 3. Schematic diagram of the 1/4 simulation domain for (a) a typical CNT-based triode-type (single gate) and (b) CNT-based tetrode-type (double gate) field emitter within a periodic cell. The important geometrical parameters are R=500 nm, r=10 nm, h_e=600 nm, h=500 nm, d=200 nm, L=0.9 mm, W=0.3 m, R_f=1.5 μm, h_1=500 nm, h_2=500 nm, d_1=200 nm, and d_2=200 nm.

The emitted electrons then move at each time step by integrating the Lorentz equation using the existing electromagnetic field.

In the present study, we have added a vertically downward magnetic field ($-B_z$), in addition to the simulated electric field, by assuming that the magnetic flux density inside each emission cell is approximately uniform in space, as shown in Fig. 1. Electron trajectory from the emitter surface to the anode surface is traced on the unstructured mesh based on the added downward magnetic field and computed electric field distribution from Poisson's equation solver, by using the cell-by-cell particle-tracking technique developed previously for direct simulation Monte Carlo simulation.[33] The anode current is then computed as the time average of the accumulated charges, due to electron flows, reaching the anode surface.

III. RESULTS AND DISCUSSION

In this article, we only simulate an individual gated CNT field emitter within a periodic cell. A quarter of the full simulation domain of a single gated cathode structure is shown in Fig. 3(a), while a typical quarter of final adaptive refined mesh (211 628 nodes) is shown in Fig. 2. Important geometrical conditions include the tip radius of 10 nm, emitter height of 600 nm, distance of 0.5 μm between the gate and cathode, gate radius of 0.5 μm above the emitter, distance of 900 μm between the anode and the cathode, thickness of the gate of 0.2 μm, and the half-width of each cell measuring 300 μm. The applied voltage of the gate ranges from 60 to 120 V, whereas the cathode and anode are grounded and applied with 1000 V, respectively.

Without the electrostatic focusing structure or externally applied magnetic focusing field, the simulated anode current versus gate voltage (*I-V*) curve is shown in Fig. 4, which displays a turn-on voltage of about 95 V. Note that the turn-on voltage is defined as the gate voltage at which the current to the anode is 1 μA. The anode current plotted in Fowler-Nordheim coordinates (FN plot) is also shown as an inset to Fig. 4. The linearity of the FN plot clearly shows that the computed *I-V* data follow the Fowler-Nordheim model very well. Note that the anode current obviously increases with increasing gate voltage, whereas, shown later (Figs. 7 and 8), the electron-beam diameter at the anode increases rapidly with increasing gate voltage, which is detrimental to the resolution requirements. The corresponding electron
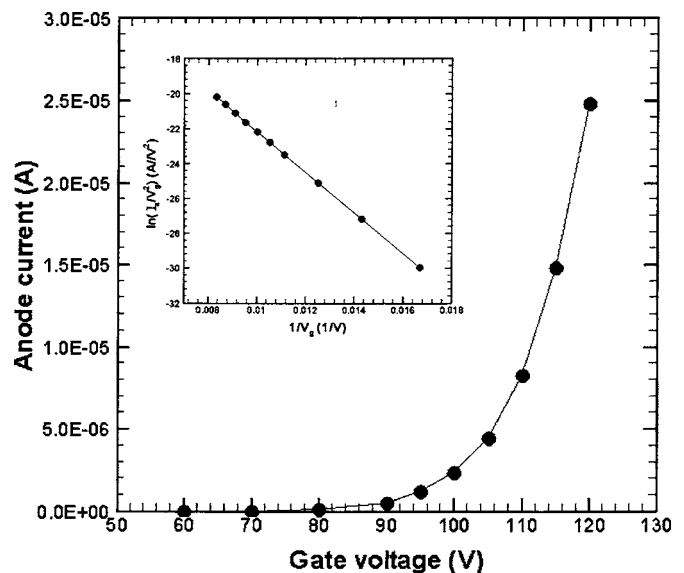

FIG. 4. Field-emission *I-V* characteristic of a single-gated CNT field emitter without the externally applied downward magnetic field.
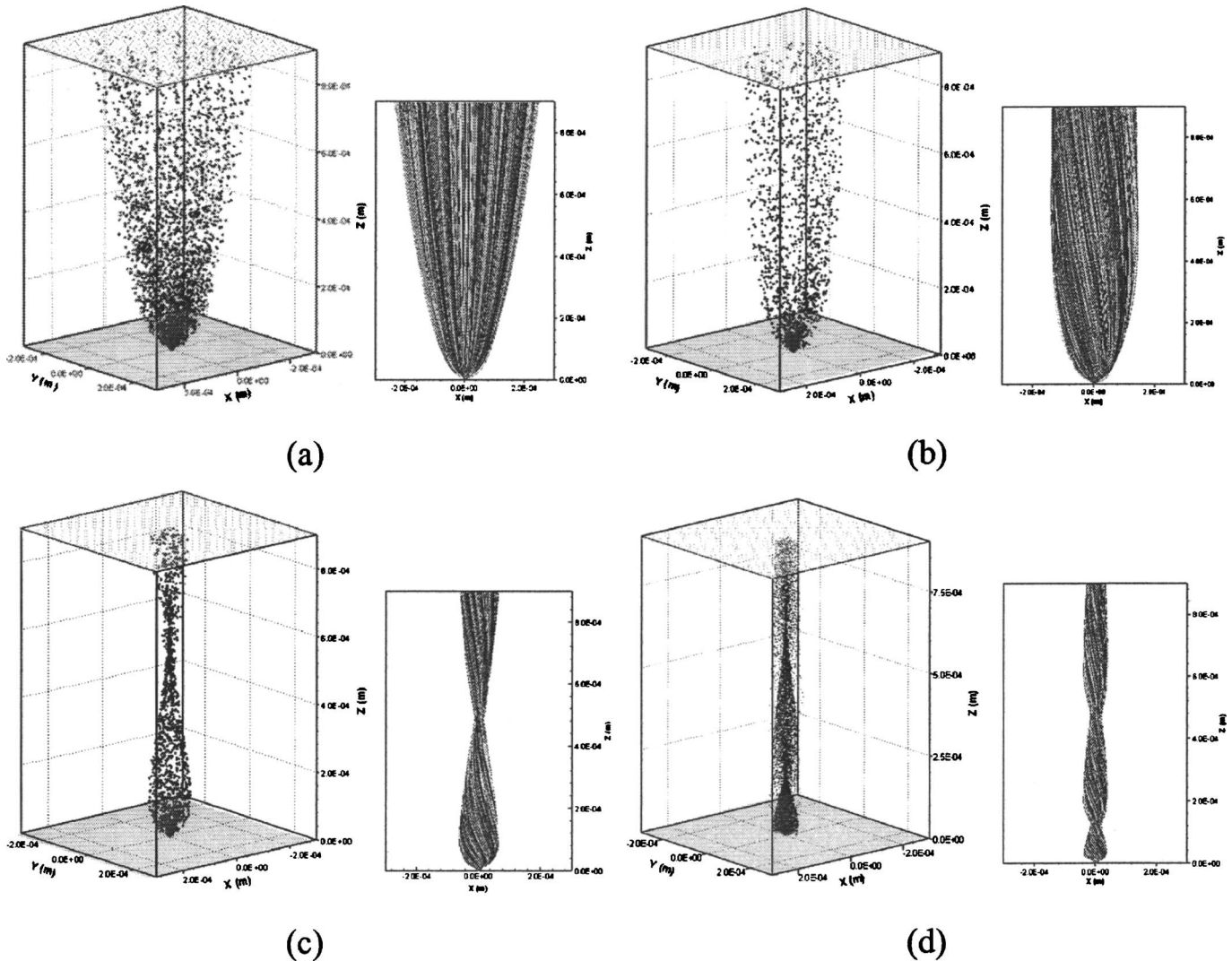
(a)

(b)

(c)

(d)

FIG. 5. Snapshots and trajectories of electrons for (a) $B_z = 0$ T, (b) $B_z = -0.2$ T, (c) $B_z = -0.5$ T, and (d) $B_z = -1.0$ T. The gate voltage and anode voltage are fixed to 120 V and 1 kV, respectively.

snapshots and trajectories with the gate voltage of 120 V are illustrated in Fig. 5(a), which will be explained shortly.

Furthermore, we simulate the electron trajectories by considering the presence of the externally applied downward magnetic field in the range of 0–0.85 T to study the influence of the magnetic field on electron focusing. In Figs. 5(a)–5(d), several 3D electron snapshots and trajectories are presented at the gate voltage of 120 V, anode voltage of 1 kV, and different magnetic flux densities of 0, −0.2, −0.5, and −1 T, respectively. In the present study, we define the electron-beam diameter as the diameter of the circular beam spot at the anode plane, within which 95% of the electrons are gathered. A typical distribution of electron number is shown in Fig. 6 for reference. Based on all the simulated electron trajectories, the maximum diameter of beam spot on the anode plane can be estimated. The dependence of electron-beam diameter for different applied gate voltages on the magnetic flux density is shown in Fig. 7, which demonstrates an Airy-function-type shape. It is also observed that electron-beam diameter generally increases with increasing

gate voltage. However, this trend becomes less pronounced at larger values of downward magnetic field intensity. This implies that, with externally applied magnetic field, a larger value of gate voltage can be used to increase the emission current without increasing the beam diameter too much.

From Fig. 8, it is clear that the electron-beam diameter rapidly decreases from 530 μm to less than 50 μm as the magnetic flux density increases from zero to −0.35 T at $V_g = 120$ V. At $B_z = -0.2$ T, the beam diameters are estimated as 268, 292, and 297 μm for the gate voltages of 80, 100, and 120 V, respectively. The results are comparable to the typical pixel size (0.25–0.35 mm) of the FEDs.[10] At $B_z = -0.35$ T, the beam spot size is estimated as 47, 49 and 52 μm for the gate voltages of 80, 100, and 120 V, respectively, which is a minimum in the present simulation conditions. The overfocusing of the electron beam, as shown in Fig. 5(c), is observed in some high magnetic flux density cases, and the oscillation amplitude in electron-beam diameter diminishes as the magnetic field becomes very large. At very large values of the magnetic field, the electron-beam size eventually
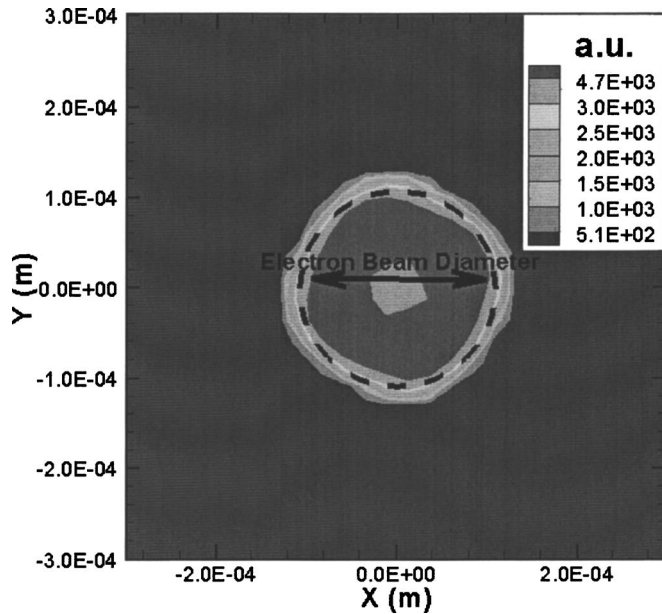
FIG. 6. Typical electron number distribution at the beam spot under the condition of $B_z=-0.25$ T, $V_g=120$ V, and $V_{anode}=1000$ V.

FIG. 7. Dependence of electron-beam diameter at the anode on the flux density of magnetic focusing field.

converges. The total emission current and anode current with magnetic focusing field are the same as the results without the magnetic field. From the simulation, we find that this magnetic focusing design can optimally suppress the electron-beam dispersion under a well-controlled magnetic field, and the emission current to the anode will not decrease by using this magnetic focusing method.

Figure 3(b) shows schematically the same field emitter as Fig. 3(a) with an additional focusing electrode placed between the gate electrode and anode, as the conventional field-emitter design does. The focusing electrode will generate a local electrostatic field to refocus the emitted electron beam. Most geometrical conditions are the same as those in Fig. 3(a), except for the following: The focusing electrode is 0.5 μm from the gate electrode, the thickness of the focusing electrode is 0.2 μm, and the radius of the central hole of the focusing electrode is 1.5 μm. The applied voltage of the focusing electrode may be positive or negative.

The typical electron trajectories corresponding to different focusing voltages $V_f=-5$, 0, and 5 V are shown in Figs. 9(a)–9(c), respectively. The results show that the focusing electrode with negative voltage ($V_f=-5$ V and $V_g=120$ V) can effectively reduce the spreading angle of the electron beams and produce well-focused electron beams. The dependence of the electron-beam diameter on focusing voltage at various gate voltage is shown in Fig. 10, which further confirms the effective reduction of beam diameter by using negative focusing voltage, in addition to the lower gate voltage. The diameter of the focused electron beams using an electrostatic focusing structure is generally small and comparable to those using magnetic focusing.

However, there are several drawbacks of the electrostatic focusing design. They include increasing difficulties of manufacturing for the focusing structure and much lower an-
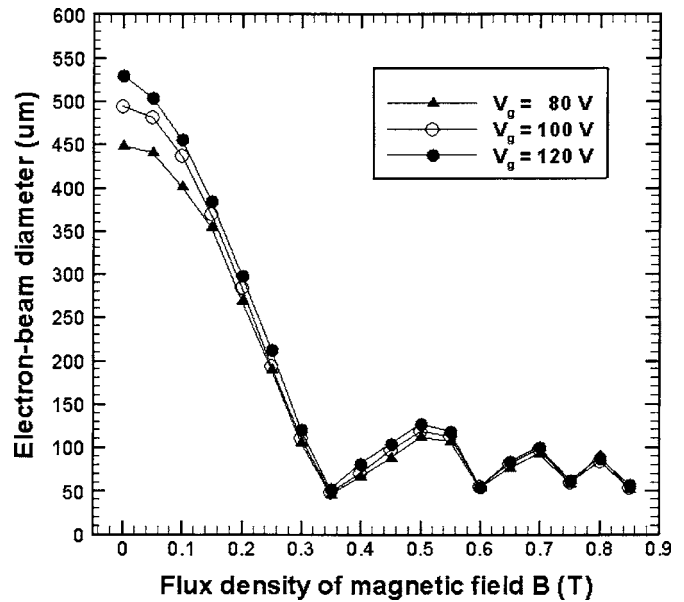
ode current due to the screening effect of this focusing structure and increasing leakage current to the gate. The latter point can be clearly seen from Fig. 11, which illustrates the dependence of anode current and gate current on focusing voltage at various gate voltages. The dramatic decrease in total emitted current from the emitter tip (e.g., 2.45 $\times 10^{-5}$ A for the triode structure reduces to 6.50×10^{-6} A for the tetrode structure with $V_f=5$ V, at $V_g=120$ V) is attributed to the reduction of electric field caused by the addition of the electrostatic focusing structure. In addition, more than 15%–45% of emitted electrons are intercepted by the gate electrode when the electrostatic focusing electrode is used.
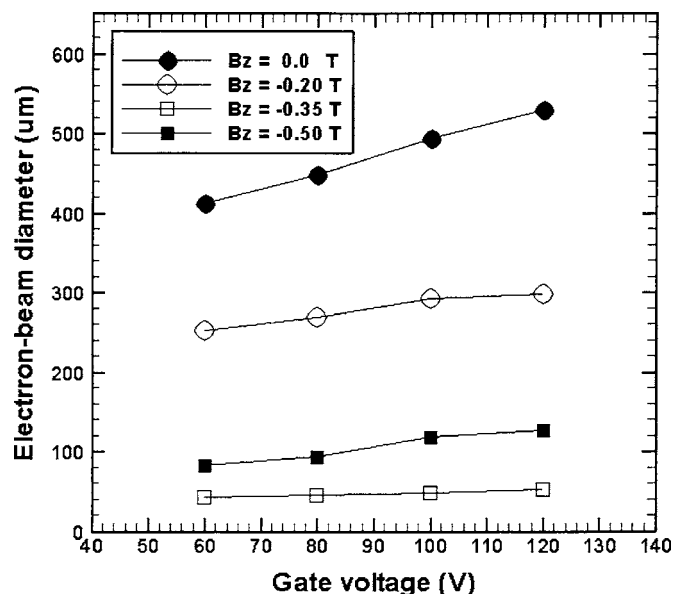

FIG. 8. Dependence of electron-beam diameter at the anode on the gate voltage for different flux densities of magnetic focusing field.
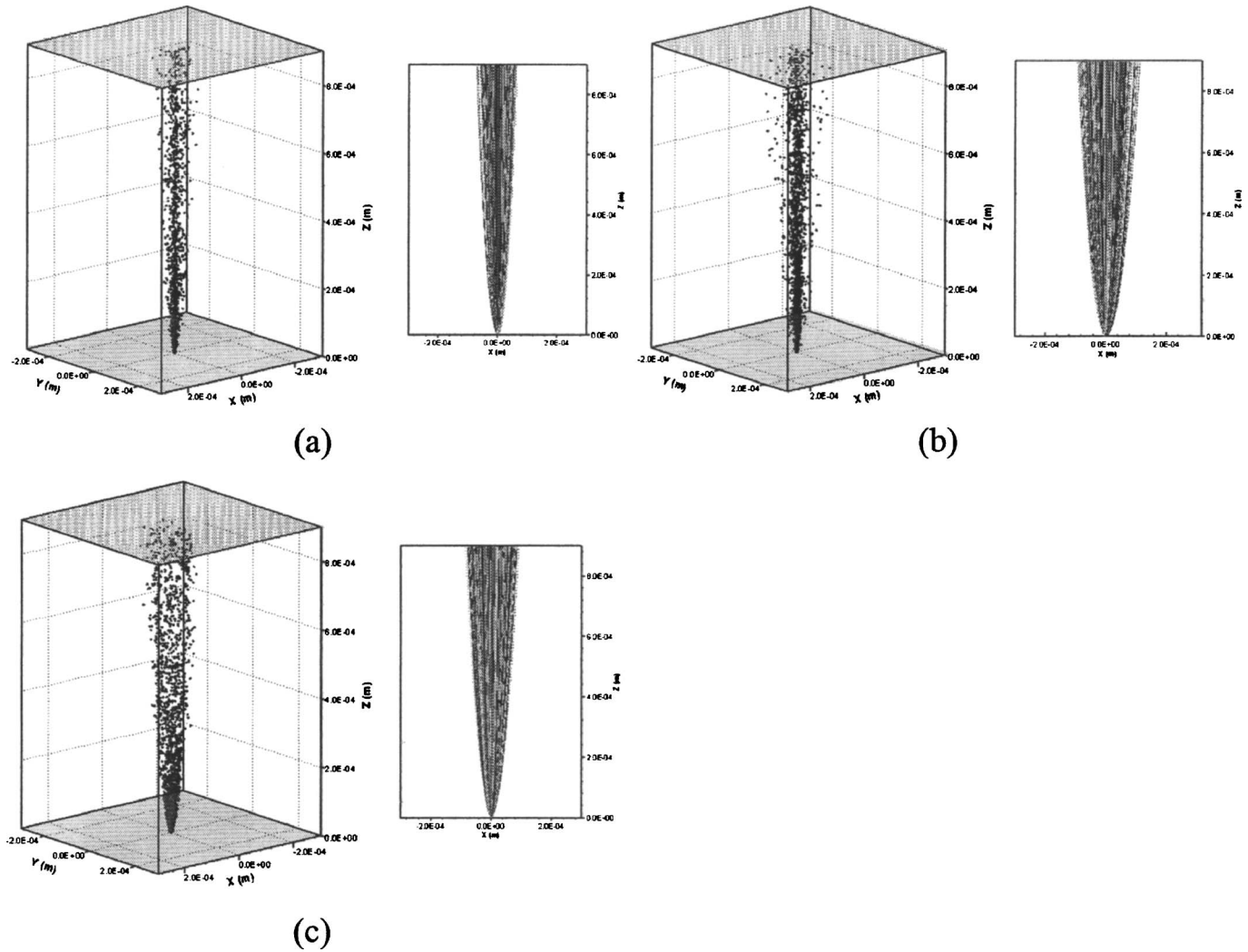
FIG. 9. Snapshots and electron trajectories without downward magnetic field. (a) $V_f = -0.5$ V, (b) $V_f = 0$ V, and (c) $V_f = +0.5$ V. The gate voltage and anode voltage are fixed to 120 V and 1 kV, respectively.

We also found that the anode current increases and gate current decreases with increasing focusing voltage due to less electric field screening, as shown in Fig. 11. The best focusing beam spot size at the anode, 97.3 μm ($V_g = 80$ V), 120.1 μm ($V_g = 100$ V), and 154.8 μm ($V_g = 120$ V) with $V_f = -5$ V is still 1.73, 2.46, and 2.98 times, respectively, larger than the spot size (46.3, 48.9, and 52.0 μm) with magnetic focusing ($B_z = -0.35$ T). If a larger emission current is required (thus, a larger gate voltage is applied), the effect of the focusing on electrons due to the focusing electrode becomes less pronounced, as shown in Fig. 10 with $V_g = 120$ V. Although we can obtain a better focused electron beam by lowering the focusing voltage, the anode current decreases with dramatically increasing the percentage of gate current. The increasing gate current consumes more input power, but it also causes possible corrosion of the gate due to electron bombardment.[9] Thus, as compared to electrostatic focusing, magnetic focusing greatly enhances the field-emission anode current, but also reduces the dispersion of
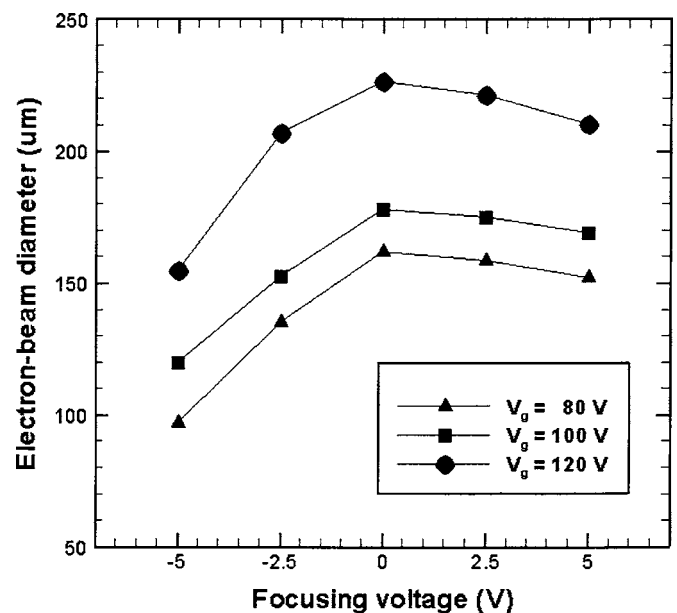

FIG. 10. Dependence of electron-beam diameter at the anode on the focusing voltage for different gate voltages.
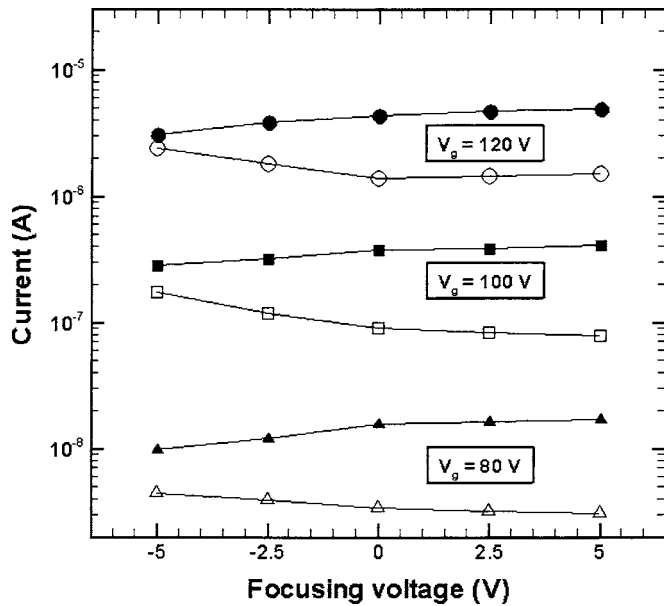
FIG. 11. Variation of anode current as a function of focusing voltage for different gate voltages: $V_g=80$ V (▲), $V_g=100$ V (■), and $V_g=120$ V (●); and gate current as a function of focusing voltage for different gate voltages: $V_g=80$ V (△), $V_g=100$ V (□), and $V_g=120$ V (○).

the beam at the anode. This, in turn, increases the efficiency of the power consumption and beam quality at the anode.

IV. CONCLUSIONS

We have simulated the field-emission properties of the triode-type field-emission device using a single CNT field emitter with a novel magnetic focusing structure and with a conventional electrostatic focusing structure for comparison. The simulation results clearly demonstrate that, with the proper magnetic focusing design, a highly focused electron beam can be produced with higher efficiency of power consumption, as compared with conventional electrostatic focusing. Considering the simplicity of fabrication as compared to electrostatic focusing, a magnetic focusing system is relatively easy to implement. A magnetic field perpendicular to the cathode substrate can be constructed by several permanent magnets or coils outside the FE devices. Two of the immediate advantages, compared to electrostatic focusing, are the reduction of the complexity in microfabricating the focus electrode and the prevention of the device-to-device uniformity problem. These verifications in the present study all confirm the benefits of this design for well-focused and high-power-efficiency electron sources for future FE applications. The major limitation of such magnetic focusing lies in the difficulty in keeping the uniformity of the magnetic field over a large area. If we just take the FE devices for applications with small size into consideration, the magnetic focusing design may provide a compromise between device performance and manufacturability. Generating a uniform downward magnetic flux within large-sized FE devices remains an active area of research.

[1]M. I. Milne *et al.*, J. Mater. Chem. **14**, 933 (2004).
[2]S. Iijima, Nature (London) **354**, 56 (1991).
[3]A. G. Rinzler *et al.*, Science **270**, 1179 (1995).
[4]A. M. Rao, D. Jacques, R. C. Haddon, W. Zhu, C. Bower, and S. Jin, Appl. Phys. Lett. **76**, 3813 (2000).
[5]S. Itoh, M. Tanaka, and T. Tonegawa, J. Vac. Sci. Technol. B **22**, 1364 (2004).
[6]L. R. Baylor *et al.*, J. Vac. Sci. Technol. B **22**, 3021 (2004).
[7]Q. H. Wang, M. Yan, and R. P. H. Chang, Appl. Phys. Lett. **78**, 1294 (2001).
[8]J. E. Jung *et al.*, J. Vac. Sci. Technol. B **21**, 1071 (2003).
[9]C. Xie, IEEE Trans. Nanotechnol. **3**, 404 (2004).
[10]J. H. Choi *et al.*, IEEE Trans. Electron Devices **52**, 2584 (2005).
[11]Y. C. Lan, J. T. Lai, S. H. Chen, W. C. Wang, C. H. Tsai, K. L. Tsai, and C. Y. Sheu, J. Vac. Sci. Technol. B **18**, 911 (2000).
[12]J. H. Choi *et al.*, Appl. Phys. Lett. **84**, 1022 (2004).
[13]L. Lie, W. Hong, Z. Jun, J. C. Wen, Y. Z. Zhang, and Y. G. Liu, IEEE Trans. Plasma Sci. **32**, 1742 (2004).
[14]K. B. K. Teo *et al.*, J. Vac. Sci. Technol. B **21**, 693 (2003).
[15]C. A. Spindt, I. Brodie, L. Humphrey, and E. R. Westerberg, J. Appl. Phys. **47**, 5248 (1976).
[16]G. Pirio, P. Legagneux, D. Pribat, K. B. K. Teo, M. Chhowalla, G. A. J. Amaratunga, and W. I. Milne, Nanotechnology **13**, 1 (2002).
[17]L. Gangloff *et al.*, Nano Lett. **4**, 1575 (2004).
[18]M. A. Guillorn, A. V. Melechko, V. I. Merkulov, E. D. Ellis, C. L. Britton, M. L. Simpson, D. H. Lowndes, and L. R. Baylor, Appl. Phys. Lett. **79**, 3506 (2001).
[19]M. A. Guillorn, A. V. Melechko, V. I. Merkulov, D. K. Hensley, M. L. Simpson, and D. H. Lowndes, Appl. Phys. Lett. **81**, 3660 (2002).
[20]D. Nicolaescu, V. Filip, and J. Itoh, Jpn. J. Appl. Phys., Part 1 **40**, 83 (2001).
[21]M. A. Guillorn *et al.*, J. Vac. Sci. Technol. B **22**, 35 (2004).
[22]J. Itoh, Y. Tohma, K. Morikawa, S. Kanemaru, and K. Shimizu, J. Vac. Sci. Technol. B **13**, 1968 (1995).
[23]A. V. Melechko, V. I. Merkulov, T. E. McKnight, M. A. Guillorn, K. L. Klein, D. H. Lowndes, and M. C. Simpson, J. Appl. Phys. **97**, 041301 (2005).
[24]N. Egami *et al.*, J. Vac. Sci. Technol. B **23**, 2056 (2005).
[25]D. Nicolaescu, V. Filip, S. Kanemaru, and J. Itoh, J. Vac. Sci. Technol. B **21**, 366 (2003).
[26]S. Bae, W. J. Seo, S. Choi, S. Lee, and K. H. Koh, J. Vac. Sci. Technol. B **22**, 1303 764 (1994).
[27]K. H. Hsu, P. Y. Chen, C. T. Hung, L. H. Chen, and J. S. Wu, Comput. Phys. Commun. **174**, 948 (2006).
[28]J. S. Wu and K.-H. Hsu, J. Plasma Phys. (to be published).
[29]Y. Saad, *Iterative Methods for Sparse Linear Systems* (Society for Industrial and Applied Mathematics, Philadelphia, 2003).
[30]G. Karypis, K. Schloegel, and V. Kumar, PARMETIS, University of Minnesota, 1998.
[31]O. C. Zienkiewicz and J. Z. Chu, Int. J. Numer. Methods Eng. **24**, 337 (1987).
[32]R. H. Fowler and L. Nordheim, Proc. R. Soc. London, Ser. A **119**, 173 (1928).
[33]J. S. Wu and Y. Y. Lian, Comput. Fluids **32**, 1133 (2003).